COLLABORATION BETWEEN DIGITAL ROCK ANALYSIS AND LABORATORY FOR GENERATION OF MULTIPHASE TRANSPORT PROPERTIES FOR RESERVOIR SAMPLES

Nasiru Idowu[1], Alessio Arena[1], Ben Young[1], Arjen Mascini[1], Kurdistan Chawshin[1], Carley Goodwin[1], Silvano Sommacal[1], Stig Bakke[1], Mark Knackstedt[1], Pål-Eric Øren[1], and Mohammad Piri[2]
[1] FEI Oil and Gas; and [2] University of Wyoming

This paper was prepared for presentation at the International Symposium of the Society of Core Analysts held in Snowmass, Colorado, USA, 21-26 August 2016.

ABSTRACT
We present a collaborative study between FEI digital rock analysis (DRA) services and University of Wyoming on poorly sorted clastic reservoir core materials. The methodology highlights a multiscale approach which features plug/sub-plug scale imaging, and submicron resolution using Backscattered Scanning Electron Microscopy (BSEM) imaging. Pore network models were generated from micron-scale sub-plug images for the resolved porosity and with a process-based reconstruction method (PBM) for the sub-resolution porosity. The pore-scale advancing contact angles were measured *in situ* and used as inputs in the simulator. The simulation results obtained from the different pore networks were upscaled using a steady-state technique for each sample. This approach enables us to generate reliable multiphase transport properties on three bi-modal sandstone reservoir samples. Simulated results are compared with available experimental data.

INTRODUCTION
In the current seemingly unending oil price slump, the oil and gas industry must be innovative and ensure optimal recovery of hydrocarbons from conventional and unconventional reservoirs at minimal costs. This requires a good understanding of the reservoir wettability, reliable static/multiphase transport properties and detailed reservoir characterizations, simulations and management. For gas/water systems [1] and oil/water water-wet cases [2, 3], DRA offers a timely alternative approach to obtain essential multiphase transport data from 3D images of rock samples and/or from simplified pore networks extracted from high resolution images. It also provides the opportunity for fast and meaningful sensitivity studies on discrete and homogeneous core material.

However, most reservoirs are neither water-wet nor oil-wet and determination of the actual wettability distribution is crucial [4]. Amott [5] or USBM [6] tests can provide

quantitative averaged wettability information of a core sample. Contact angle, however, is the most universal measure of the wettability of surfaces [4]. Andrew *et al*. [7] recently presented a method for contact angle measurement from X-ray micro-computed tomography (MCT) of a supercritical CO_2-brine system in a Ketton limestone with simple mineralogy (comprising 99.1% calcite and 0.9% quartz). Qualitative pore-scale distribution of wettability has also been obtained by integrating information from MCT, Field Emission Scanning Electron Microscopy (FESEM), and Quantitative Evaluation of Minerals by SEM (QEMSCAN) [8]. With detailed information on the pore-scale distribution of wettability [8] or the pore-scale distribution of contact angles [7, 9], reliable multiphase flow properties can be generated through DRA for non-water-wet cases.

In this paper, we present a collaborative study between FEI DRA services and University of Wyoming state-of-the-art laboratory to generate single- and multiphase transport properties for three bi-modal sandstone reservoir samples. The pore-scale advancing contact angles were measured *in situ* and ranged from 90^o to 128^o using similar procedure to those stated in [9]. These were used as inputs in a quasi-static pore network simulator [3] and by so doing, we reduced uncertainties associated with wettability characterization at the pore-scale and thereby improved the reliability of the predicted data. We explored one of the strengths of DRA further and generated sensitivity analysis of the predicted data to different scenarios that would otherwise, have taken years to accomplish in the laboratory. Finally, we compared simulated results with available experimental data.

IMAGE ACQUSITION AND ANALYSIS

In the original program, twelve conventional plugs were extracted from unpreserved core material of a clastic reservoir and were characterized texturally and mineralogically. They were imaged by MCT using a HeliScan micro-CT system. Three of these plugs were chosen for the study of multiphase flow properties based on their importance to the reservoir, their specific rock typing and the quality of the reservoir material. An analysis workflow incorporating conventional and imaging laboratory techniques with DRA techniques was designed to obtaining the desired results in a timely manner, while optimizing the costs. A schematic diagram of this workflow is shown in Figure 1.

The three chosen plugs - most relevant to the reservoir-planning scenario - exhibit different depositional facies, degrees of heterogeneity, different sorting and grain size. Differences are also noted when comparing measured RCA data: porosities and permeabilities range from 21% and 768mD for *Plug* 3 to 28% and 16.8mD for *Plug* 1. Petrographically, *Plug 1* is a poorly sorted sandstone/siltstone (fine silt to very fine sand) with abundant microporous pore filling material – Figure 2. The microporous phase is dominated by micro crystalline quartz and illite. The Backscattered Electron (BSE) images indicate that a significant part of the porosity is associated with the microporous phase.

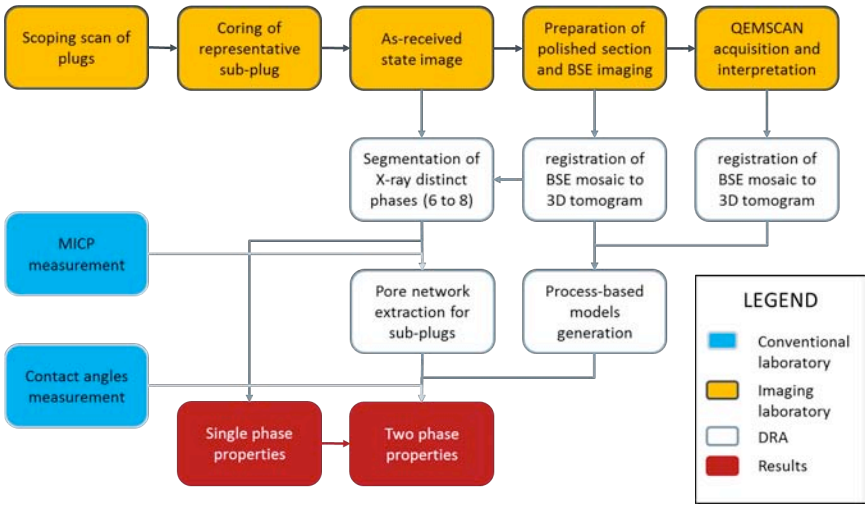

Figure 1. Analysis workflow used for this study

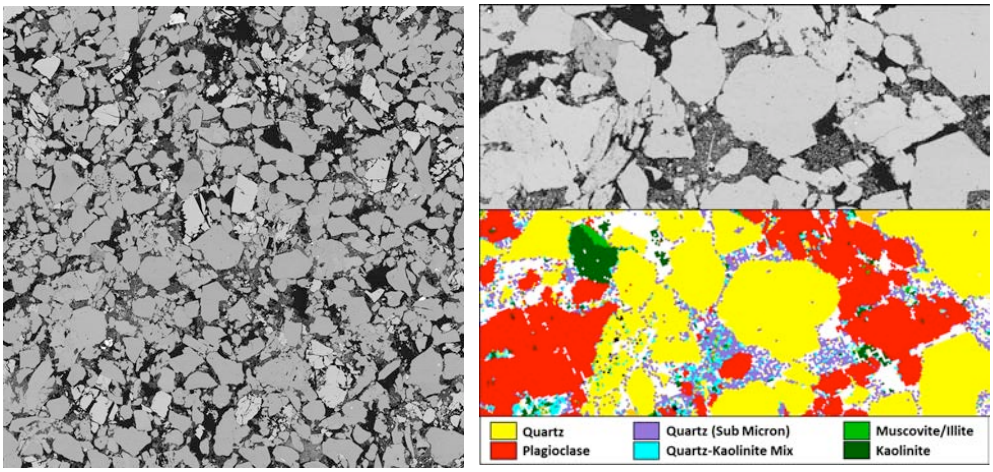

Figure 2. BSE image of plug 1, side length is 1 mm. Right: detail of BSE image and QEMSCAN map showing the mineralogical nature of the pore filling material and framework grains

Plug 2 is a poorly sorted sandstone/siltstone (medium silt to medium sand) with medium to poorly rounded grains with some pore filling microporous phase – Figure 3. The microporous phase consists of kaolinite booklets, micro crystalline quartz, illite and some carbonate/pyrite.

Plug 3 is a sandstone with a distinct unimodal grain size distribution – Figure 4 and Figure 7. Medium to coarse well rounded sand grains are surrounded by coarse silt to fine sand infill. Small amounts of microporous phase are dominated by kaolinite booklets.

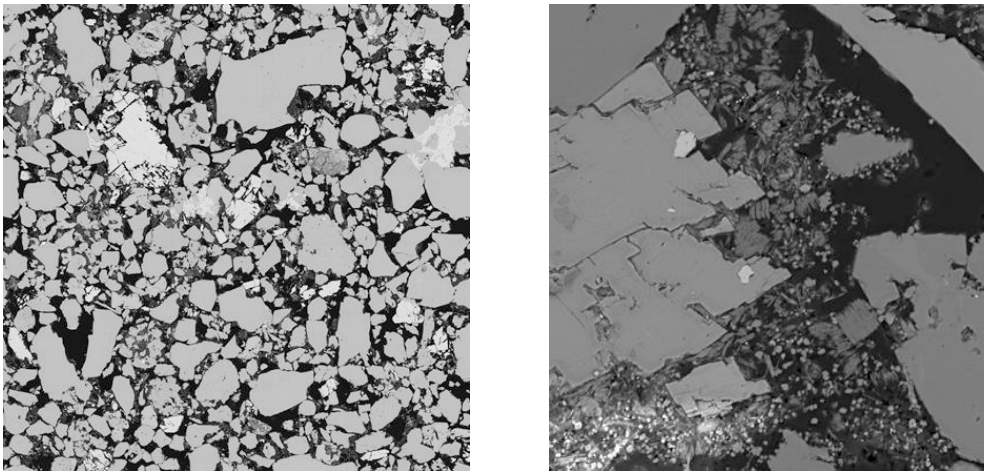

Figure 3. Left: BSE image of plug 2, side length is 2.5 mm. Right: Pore filling material

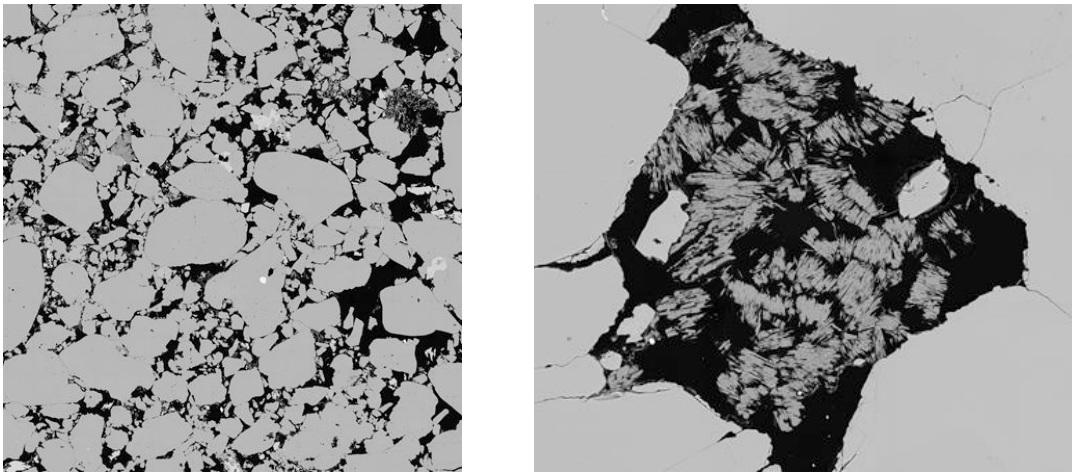

Figure 4. Left: BSE image of plug 3, side length is 5mm. Right: Pore filling kaolinite booklets

The textural differences of those samples led us to use specific coring diameter when extracting representative sub-plugs. This decision was taken in the attempt to capture a representative elementary volume (REV) estimated as 15 times the largest observed grain while maximizing the imaging resolution. Table 1 summarizes the coring diameter, length and image voxel size for each plug. Acquired images were segmented into X-ray distinct phases (up to 8 identified phases) using codes based on the converging active contour algorithm [10]. The dimensions of those images are approximately 1500 voxels in the *x* and *y* direction, and 3000 to 6000 voxels in the *z* direction; the file size is approximate 16 to 32 GB of data per image. One vertical slice for each of the three samples is shown in Figure 5. Table 2 describes the partitioning of the 3D image into porosity, microporous pore filling material, mineral grains and high density inclusions. For each of the samples, we extracted an additional 8mm sub-plug used to generate laboratory MICP data.

Table 1: Sub-plugs extraction/coring diameter, length and image voxel size for each sample

Sample	Coring diameter (mm)	Length (mm)	Voxel size (μm)
Plug 1	3	9	2.2
Plug 2	4	8	2.9
Plug 3	8	16	5.5

Sub-plugs were subsequently embedded in resin and then cut to prepare a polished section. This was imaged and analyzed by electron microscopy techniques such as BSE and Secondary Electron (SE) high magnification imaging. The mosaics of images and mineralogical maps produced in this way were registered back to the tomogram using a proprietary algorithm [11]. This enables one to directly quality check (QC) the image quality and segmentation undertaken on the 3D tomogram to higher resolution BSE data. In Figure 6, a segmented dataset (3 micron voxel sizes) is registered to a BSE image (500 nm pixel size). The segmentation into 8 phases undertaken in the 3D tomogram correlates well to solid, microporous and open porosity regions observed in the BSE images.

Table 2. Results from the segmentation of X-ray distinct phases performed on sub-plug μCT images

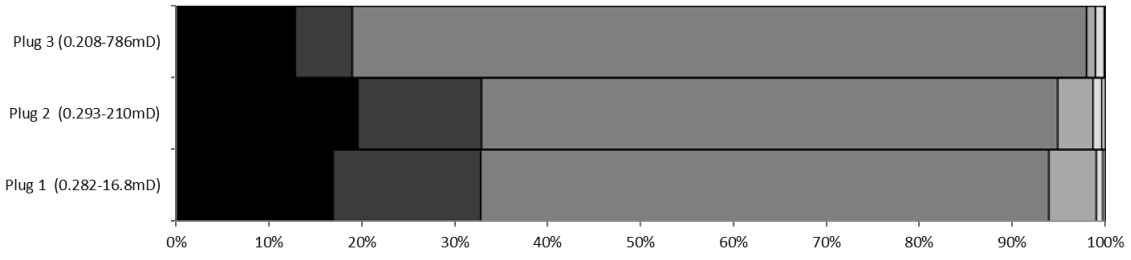

	Plug 1 (0.282-16.8mD)	Plug 2 (0.293-210mD)	Plug 3 (0.208-786mD)
Pores	16.9	19.6	12.8
Pore-filling material	15.8	13.3	6.2
Quartz	61.1	61.9	78.9
Feldspar	5.1	3.8	1
Calcite	0.7	1	0.9
High density minerals	0.2	0.3	0.1

RESULTS

Single-Phase Properties and MICP

We compute absolute permeability via imaged-based single-phase lattice Boltzmann permeability simulation. This technique only considers flow along the resolved pore pathway - through the macropores in the image; the percolation condition was met for all three sub-plugs based on the careful choice of resolution to target for our X-ray tomograms. Estimated porosities and calculated absolute permeabilities were then compared to the experimental laboratory measurement to check the relevance of the sub-region chosen compared to the original plug scale. Comparison of the experimentally derived data and image based results are shown in Table 3.

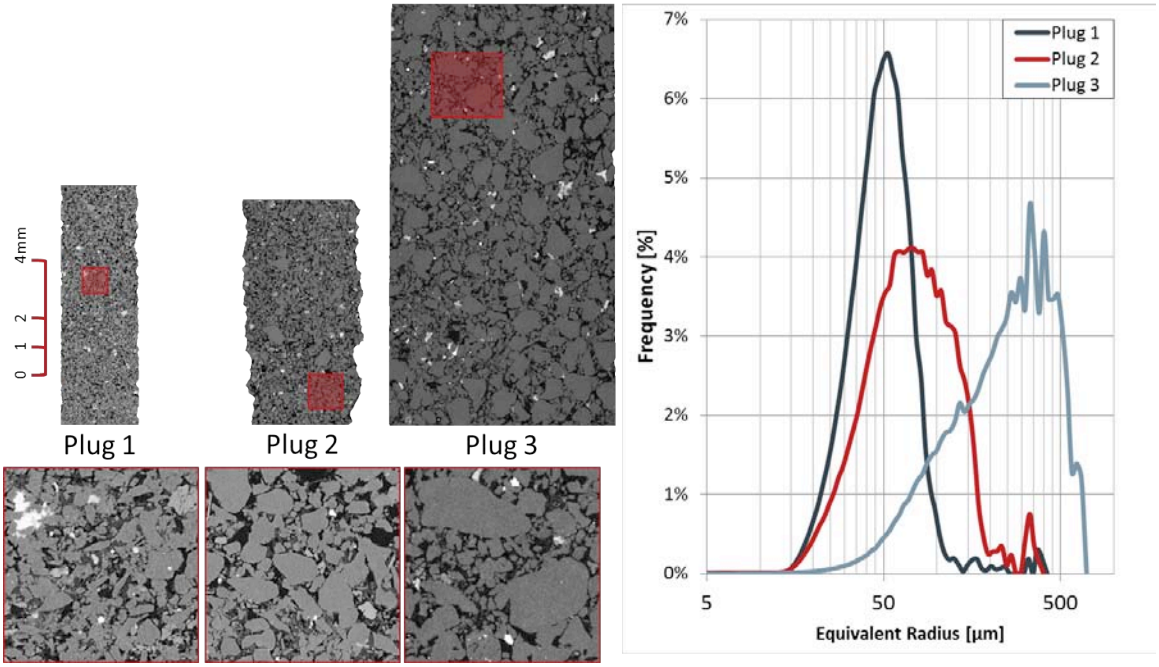

Figure 5. Vertical slices extracted from the sub-plug tomograms, plus zoom in of the highlighted region in red. The scale represented is valid only for the vertical slice. On the right: grain size distribution of the three samples calculated from X-ray tomograms as radius of the equivalent sphere

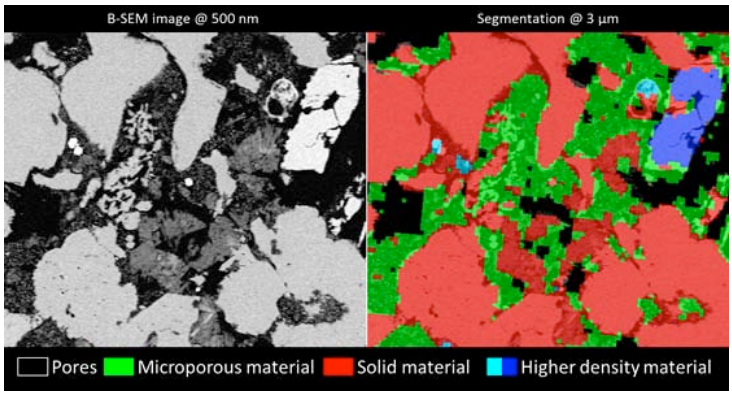

Figure 6. Visual comparison between a BSE image of the polished section prepared within the field of view of the tomogram and the corresponding horizontal slice from the segmentation result

Table 3. Comparison between laboratory measurement and digital results for porosity and absolute permeability for all three samples

Sample	Porosity (fraction)			Absolute permeability (mD)	
	RCA - plug	MICP – sister sub plug	µCT - sub-plug	RCA - Plug	µCT - sub-plug
Plug 1	0.282	0.278	0.246	16.8	62
Plug 2	0.293	0.267	0.287	210	225
Plug 3	0.208	0.18	0.175	786	660

Differences in the RCA plug and μCT sub-plug porosity varies from 0.06 to 3.6 porosity units. *Plug* 1 has the highest difference in porosity and a factor of approximately 3.7 between the measured (on plug) and computed permeability (on sub-plug). These differences may be due to highly heterogeneous nature of *Plug* 1. Measured and computed values for plugs 2 and 3 agree reasonably well. While a QC for prediction of permeability requires one to resolve only the largest hydraulic path, other properties like resistivity, formation factor and two phase properties require one to resolve most of the accessible pore systems. In Figure 7 we report MICP measurements performed on sister plugs to the samples used in the imaging process. The grey vertical lines represent the approximate resolution of the 3D tomograms. This illustrates the porosity that is identified/resolved in the tomogram and is transformed into simplified pore networks [12], which are used directly as inputs to a quasi-static flow simulator [3] for each plug.

Figure 7 also illustrates the significant contribution of the microporous regions to the total porosity. The results mirror the image data acquired in the previous section-- one cannot directly resolve a significant proportion of the porosity in the plugs 1 and 2 from tomography alone and one must incorporate information about the microporous regions in any forward modelling program. For these sub-resolution regions, tomography and segmentation information enables one to identify the spatial distribution of the microporous phase in 3D. The nature of this microporous material is then determined using the high resolution BSE information in (Figure 2 - Figure 4) to develop process and statistically-based methods to mimic the 3D structure of the microporous zones in the image. The PBM algorithms are based on simulation of the geological processes by which the rock was formed; sedimentation, compaction, and diagenesis [13]. Pore networks are also generated for these sub-resolution pores.

Primary Drainage and Waterflooding Simulation Results

Before simulating oil/brine displacement processes and generating the desired transport properties, we first establish for each rock sample whether the extracted pore networks from MCT images and PBM are representative or not. This is achieved by simulating oil/brine primary drainage on the pore networks and then upscaling [14] the resulting network-predicted oil/brine $P_c - S_w$ curves from the different networks for each sample. The upscaled oil/brine $P_c - S_w$ curve for each sample is then compared with measured mercury capillary pressure data on sister samples as shown in Figure 8 for *Plug* 2. The experimental capillary pressure data are scaled to oil/brine $P_c - S_w$ curves using interfacial tensions and contact angles in Table 4. The match between the simulated and measured data is good and confirms that the different pore classes are well captured and the networks are representative.

The oil/brine primary drainage capillary pressure simulation results shown in Figure 8 were stopped at 10 bar to match the entire MICP curves. However, based on the estimated capillary pressure values using oil and brine density and height above the oil-water-contact, the primary drainage simulations were re-run and stopped at a maximum capillary pressure of 2 bar and then followed by waterflooding. The average pore-scale advancing contact

angle of 109^{o} measured *in situ* at University of Wyoming, USA was used as input [5]. For this case, we assume 80% of all pores/throats invaded by oil during primary drainage changed wettability from initial water-wet state to oil-wet condition and investigate sensitivity analysis of the results to different percentages. Oil-wet advancing contact angles for the oil-wet pores/throats are distributed between 100^{o} to 118^{o}. For the remaining water-wet pores/throats, the advancing angles are distributed between 30^{o} to 70^{o}. Figure 8 depicts the primary drainage (PD) and waterflooding (WF) capillary pressure curves and relative permeability results for *Plug* 2. The end-point saturations and relative permeability values for all the three samples are summarized in Table 5.

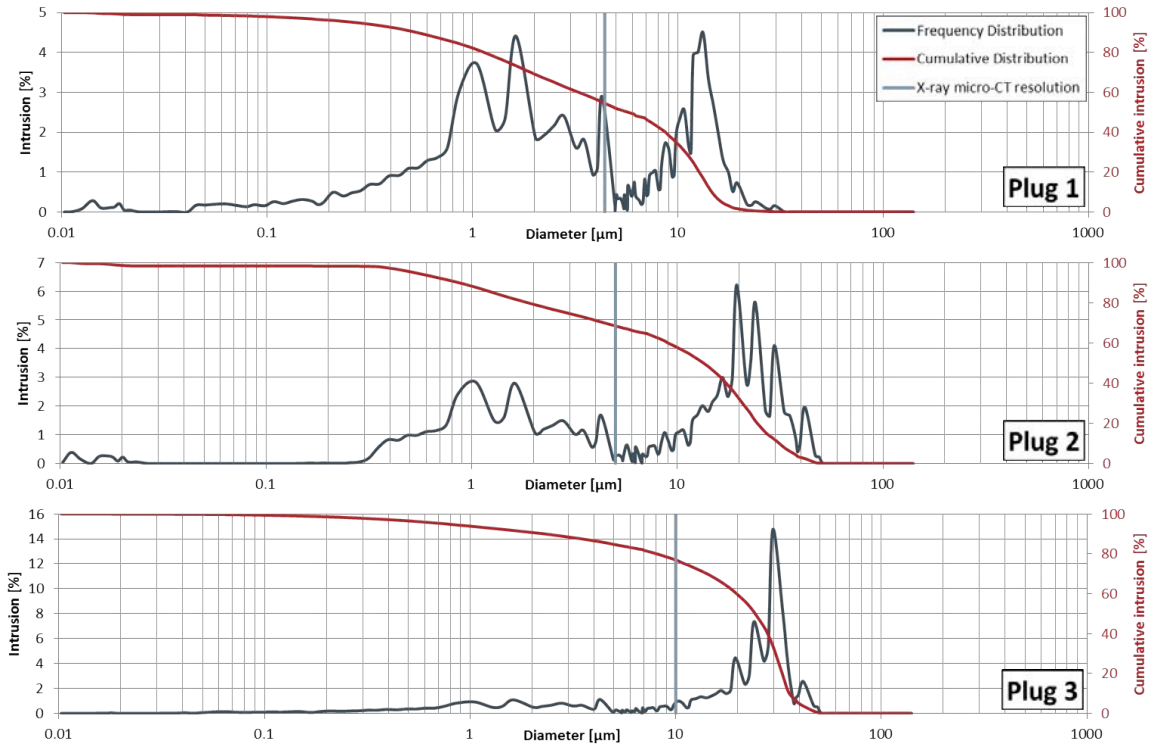

Figure 7 MICP measurement for sister plugs of the three samples studied. The black curve represents the pore size distribution, the red is the cumulative one. The vertical line is the approximate resolution of our tomograms.

Table 4: Input data to flow simulations

Water density	[kg/m^3]	**1000**
Oil density	[kg/m^3]	**700**
IFT$_{oil/brine}$	[dynes/cm]	**30**
IFT$_{Hg/air}$	[dynes/cm]	**480**
Water-wet receding angles	[degr.]	**0° – 10°**
Water-wet advancing angles	[degr.]	**30° – 70°**
Oil-wet advancing angles	[degr.]	**100° – 118°**
Mercury/air contact angles	[degr.]	**140°**
Percentage of oil-wet pores/throats		**80**

Table 5: Measured and simulated end-point saturations and relative permeability values

Property	Measured	Simulated		
		Sample 1	Sample 2	Sample 3
Porosity (fraction)	0.27	0.24	0.25	0.19
Permeability (mD)	130 – 160	93	286	814
Swi (fraction)	0.16	0.18	0.15	0.04
Kro@Swi	0.74	0.98	0.99	0.99
Sorw	0.26	0.32	0.28	0.20
Krw@Sorw	0.28	0.25	0.45	0.40

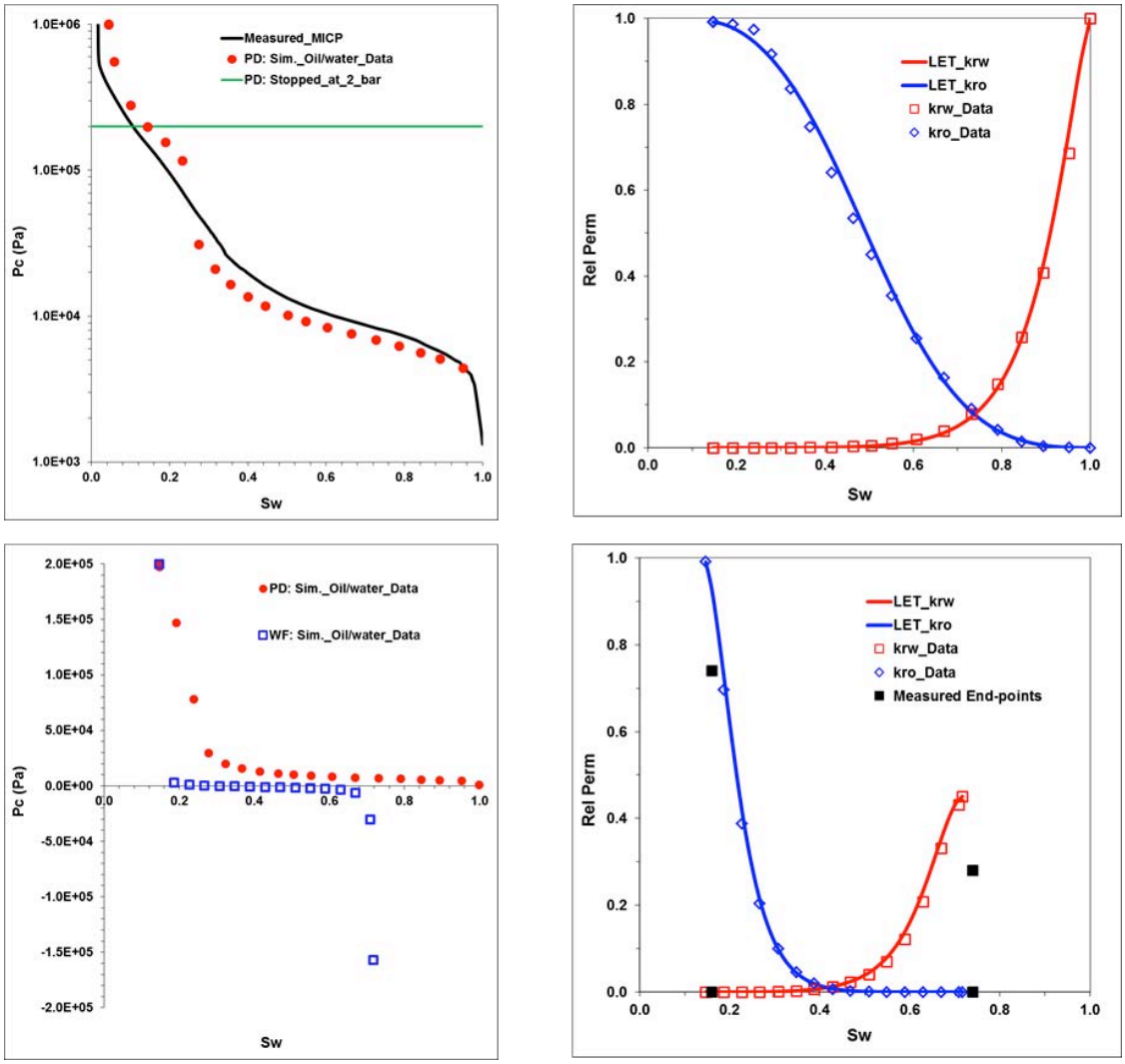

Figure 8: capillary pressure and relative permeability curves for primary drainage (top) and waterflooding (bottom) for Sample 2.

Comparison of Simulated Results to Measured Data and Sensitivity Analysis
Capillary pressure and relative permeability data were not measured during the experiments at University of Wyoming. However, porosity, permeability, end-point saturations and end-point relative permeability to water at residual oil saturation were measured on a preserved sample adjacent to sample 2 plug using unsteady-state method. Figure 8 shows the measured end-point values while Table 4 compares the simulated results with measured data. There are good agreements between measured and simulated initial water saturation and residual oil saturation despite the differences in porosity and permeability values. However, lower measured end-point relative permeability values may be due to uncertainties in measured absolute permeability values (130 -160 mD).

DRA enables one to investigate the sensitivity of the simulated results to the percentage of all pores/throats that changed wettability from initial water-wet state to oil-wet condition. We investigated this by running simulations for completely water-wet and oil-wet cases. The percentage of all pores/throats that changed wettability from initial water-wet state to oil-wet condition is 0% and 100% for water-wet and oil-wet case respectively. Oil-wet advancing contact angles for the oil-wet pores/throats are distributed between 140^o to 170^o for the completely oil-wet case while the advancing angles for the completely water-wet case remained the same (30^o to 70^o). The results of the sensitivity analysis compared with the waterflooding results presented in the previous subsection (base case) are shown in Figure 9.

Discussion of Results
The field scale implications of the relative permeability curves depicted in Figure 9 in terms of recovery is investigated using one-dimensional Buckley-Leverett analysis [15]. Assuming oil/brine viscosity ratio of 2, Figure 10 shows recovery as a function of pore volume of water injected. This figure highlights the importance of using appropriate multiphase transport data generated with correct pore-scale distribution of wettability. This will ensure good planning and forecasting and optimal recovery of hydrocarbons at minimal costs.

CONCLUSIONS
Uncertainties associated with wettability characterization at the pore-scale during DRA can be eliminated by the use of *in situ* contact angle measurements. Integration of detailed information on the pore-scale distribution of contact angles with topologically equivalent networks can guide network modelling of multiphase transport properties and considerably improve reliability of predicted results. For non-water-wet systems, we advocate an analysis workflow that incorporates conventional and imaging laboratory techniques with DRA techniques for generation of desired multiphase transport properties.

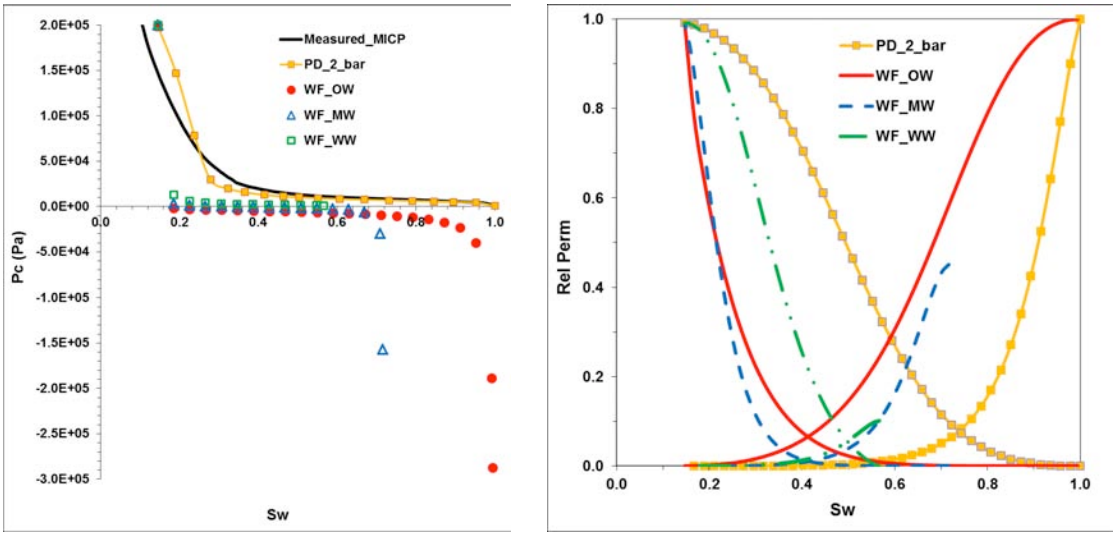

Figure 9: Capillary pressure and relative permeability sensitivity analysis waterflooding results for oil-wet (WF_OW), base case – mixed-wet (WF_MW) and water-wet (WF_WW)

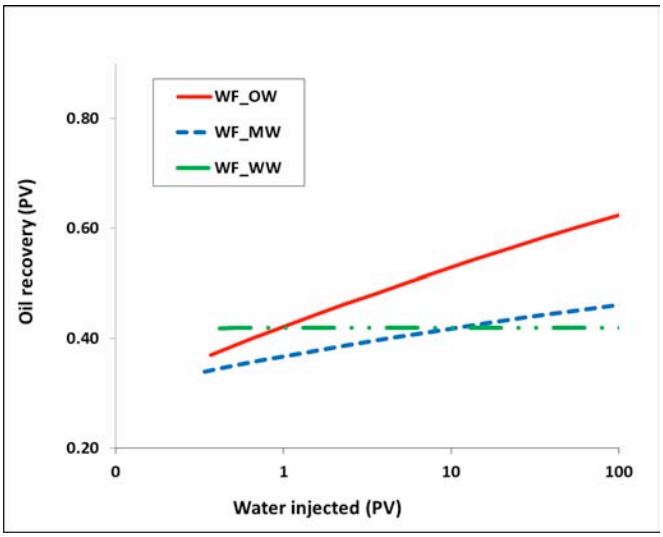

Figure 10: Oil recovery in pore volume (PV) versus PV of water injected using 1-D Buckley-Leverett analysis for the relative permeability curves depicted in Figure 9

ACKNOWLEDGMENTS

The authors acknowledge FEI Oil and Gas Business for permission to publish this paper and Hess Corporation, USA for allowing us to publish these data on their samples.

REFERENCES

1. Farokhpoor, R., Westphal, E., Idowu, N., *et al.*, "Gas-water steady-state relative permeability determination with two approaches: experiment and digital rock analysis, strengths and weaknesses", Paper SCA2016-Temp_137, Proceedings of the 2016 SCA Symposium, Snowmass, Colorado, USA, 21 - 26 August, 2016.

2. Bakke, S., and P.E. Øren, "3-D pore-scale modelling of sandstones and flow simulations in the pore networks," *SPE Journal*, (1997), **2**, 136-149.
3. Øren, P.E., S. Bakke, and O.J. Arntzen, "Extending Predictive Capabilities to Network Models", SPE Journal, (1998), **3**, 324-336.
4. Morrow, N.R., "Wettability and its Effects on Oil Recovery", *J. Pet. Tech.* (1990), **42**: 1476-1484.
5. Amott, E., "Observations Relating to the Wettability of Porous Rock", *Trans. AIME*, (1959), **216**: 156-162.
6. Donaldson, E.C., Thomas, R.D. and Lorenz, P.B., "Wettability Determination and its Effect on Recovery Efficiency", *SPE Journal*, (1969) **9**: 13-20.
7. Andrew, M., Bijeljic, B., and Blunt, M.J., "Pore-scale Contact Angle Measurements at Reservoir Conditions Using X-ray Microtomography", *Advances in Water Resources*. (2014), **68**: 24-31.
8. Idowu, N., Long, H., Øren, P.E., *et al*., "Wettability analysis using micro-CT, FESEM and QEMSCAN and its applications to digital rock physics", Paper SCA2015-010, Proceedings of the 2015 SCA Symposium, St. John's Newfoundland and Labrador, Canada 16-21 August, 2015.
9. Aghaei, A., and Piri, M., "Direct pore-to-core up-scaling of displacement processes: Dynamic pore network modelling and experimentation", Journal of Hydrology, (2015), **522**, 488-509.
10. Sheppard, A.P., Sok, R.M. and Averdunk, H., "Techniques for Image Enhancement and Segmentation of Tomographic Images of Porous Materials", Physica A (2004), 339 (1-2), 145-151.
11. Latham, S, Varslot, T and Sheppard, A., "Image registration: Enhancing and Calibrating X-ray Micro-CT Imaging", Paper SCA2008-35, Proceedings of the 2008 SCA Symposium, Abu Dhabi, UAE, 29 October – 2 November, 2008.
12. Idowu, N., Nardi, C., Long, H., *et al*., "Pore-Scale modelling: Effects of network properties on predictive capabilities", Paper SCA2012-35, Proceedings of the 2012 SCA Symposium, Aberdeen, Scotland, UK, 27-30 August, 2012.
13. Øren, P.E. and Bakke, S., "Process Based Reconstruction of Sandstones and Prediction of Transport Properties", *Transport in Porous Media*, 2002, **46**, 311-343
14. Lopez, O., Mock, A., Øren, P.E., *et al*., "Validation of Fundamental Carbonate Reservoir Core Properties Using Digital Rock Physics" Paper SCA2012-19, Proceedings of the 2012 SCA Symposium, Aberdeen, Scotland, UK, 27-30 August, 2012.
15. Buckley, S.E., and Leverett, M.C., "Mechanisms of fluid displacement in sands", Trans. AIME, (1942), **146**, 107–116